nature materials

Article

https://doi.org/10.1038/s41563-023-01619-9

Ferroelectricity in hafnia controlled via surface electrochemical state

In the format provided by the authors and unedited

Table of Contents

A. Landau-Ginzburg-Devonshire-Stephenson-Highland (LGD-SH) approach

For ferroelectric-semiconductor interfaces nonlinear screening phenomena can be critically important. A thermodynamic approach for ultrathin ferroelectric film in equilibrium with a chemical environment that supplies positive and negative charge species to compensate its polarization bound charge at the surface was developed by Stephenson and Highland (SH) [i, ii]. We modified the SH approach allowing for the presence of a gap between the ferroelectric surface covered by ions and a SPM tip [iii, iv, v, vi] and developed the analytical description for thermodynamics and kinetics of these systems. The emergent behaviors in uniaxial antiferroelectric-ferroelectric (AFE-FE) thin films covered with surface ions have been explored within the framework of the Landau-Ginzburg-Devonshire-Stephenson-Highland (LGD-SH) approach [vii]. The approach allows the characterization of the polar and anti-polar orderings dependence on the voltage applied to the film, and the analysis of their static and dynamic hysteresis loops.

Below we use the LGD-SH formalism for the description of polar and anti-polar orderings in the HZO films covered by surface ions with a charge density proportional to the relative partial oxygen pressure.

B. Geometry and basic equations

Geometry of the considered system, consisting of electron conducting bottom electrode, HZO film of thickness h, screening layer with charge density $\sigma(\phi)$, and ultra-thin gap of thickness λ separating the film surface and the tip electrode, is shown in **Fig. S1**. Note that the ferroelectric HfO_2 thin films useful for electronics application usually have a top electrode, and the properties of the electric contact at the top and bottom electrodes are different due to the difference in their deposition conditions. Relatively often the bottom electric contact is ideal, while the top contact may contain an ultra-thin dielectric gap, or the thin subsurface layer of the HfO2 film transforms into a so-called passive or "dead" dielectric layer [viii, ix, x], or the density of states at the top interface/surface differs from the one at the bottom interface/surface of the film. For all above cases, presenting an "electrically-asymmetric" heterostructure, the consideration of the model situation of the electrically-open "bare" top surface separated from the tip electrode by and an

ultra-thin gap, and ideally electrically-closed bottom surface is a reasonable case describing possible asymmetry of existing electric boundary conditions.

The linear equation of state $\boldsymbol{D} = \varepsilon_0 \varepsilon_d \boldsymbol{E}$ relates an electric displacement $\boldsymbol{D}$ and field $\boldsymbol{E}$ in the gap between the top electrode and the surface of the HZO film. Here ε_0 is a universal dielectric constant and $\varepsilon_d \cong 1$ is a relative permittivity in the gap filled by an air with controllable oxygen pressure. In the HZO film the displacement $\boldsymbol{D} = \varepsilon_0 \varepsilon_b \boldsymbol{E} + \boldsymbol{P}$, and ε_b is a relative background permittivity of antiferroelectric, $\varepsilon_b \leq 10$ [xi].

The electric field E_i is related with electric potential ϕ in a conventional way, $E_i = -\frac{\partial \phi}{\partial x_i}$. A potential ϕ of a quasi-static electric field inside the film satisfies a Laplace equation in the gap and a Poisson equation in the film, with the bound charge density determined by the polarization gradient. The boundary conditions for the system are the equivalence of the electric potential to the applied voltage U at the top electrode (modeled by a flattened region $z = -\lambda$); and the equivalence of the difference $D_3^{(gap)} - D_3^{(film)}$ to the ionic surface charge density $\sigma[\phi(\vec{r})]$ at $z = 0$; the continuity of the ϕ at gap - film interface $z = 0$; and zero potential at the conducting bottom electrode $z = h$.

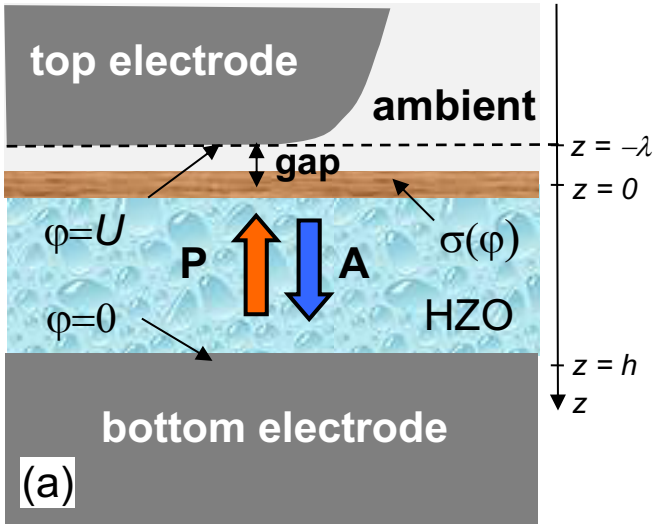

Figure S1. Geometry of the considered system, consisting of electron conducting bottom electrode, HZO film of thickness h, screening layer with charge density $\sigma(\phi)$, and ultra-thin gap of thickness λ separating the film surface and the tip electrode.

To the best of our knowledge, persuasive evidence of the AFE instability exitance in their HZO films are absent to date, however the AFE-type phase is likely to appear in ZrO_2 at room temperatures. Properly treated HfO_2 is a ferroelectric material. Hence, we can suggest that HZO contains the FE and AFE components, HfO_2 and ZrO_2. Therefore HZO free energy can be treated similarly to the energy of $(Pb,Zr)TiO_3$ compound considered by Haun et al. [xii, xiii], who presented the free energy of $(Pb,Zr)TiO_3$ as a solid solution of two materials, a ferroelectric (FE) $PbTiO_3$ and an antiferroelectric (AFE) $PbZrO_3$. Using the analogy, the free energy for HZO also should contain the FE and AFE components, HfO_2 and ZrO_2. Thus, to determine the spatial-temporal evolution of polarization components in the HZO film we use Kittel-type model [xiv] incorporating anti-polar modes related oxygen octahedral rotations [xv, xvi, xvii] combined with the LGD approach. Corresponding LGD free energy functional F additively includes a bulk part – an expansion on even powers of the polarization (P_i) and anti-polarization (A_i), F_{bulk}; a polarization gradient energy contribution, F_{grad}; an electrostatic contribution, F_{el}; and a surface energy, F_S. It has the form:

$$F = F_{bulk} + F_{grad} + F_{el} + F_S, \tag{1}$$

where the constituent parts are

$$F_{bulk} = \int_{V_f} d^3r \left(\frac{a_i}{2}P_i^2 + \frac{a_{ij}}{4}P_i^2P_j^2 + \frac{a_{ijk}}{6}P_i^2P_j^2P_k^2 + \frac{\chi_{ij}}{2}P_i^2A_j^2 + \frac{b_i}{2}A_i^2 + \frac{b_{ij}}{4}A_i^2A_j^2 + \frac{b_{ijk}}{6}A_i^2A_j^2A_k^2\right), \tag{2a}$$

$$F_{grad} = \int_{V_f} d^3r \frac{g_{ijkl}}{2}\left(\frac{\partial P_i}{\partial x_j}\frac{\partial P_k}{\partial x_l} + \frac{\partial A_i}{\partial x_j}\frac{\partial A_k}{\partial x_l}\right), \tag{2b}$$

$$F_{el} = -\int_{V_f} d^3r \left(P_iE_i + \frac{\varepsilon_0\varepsilon_b}{2}E_iE_i\right), \tag{2c}$$

$$F_S = \frac{1}{2}\int_S d^2r\, a_{ij}^{(S)}\left(P_iP_j + A_iA_j\right). \tag{2d}$$

Here V_f is the film volume. The coefficients a_i and b_i linearly depends on temperature T; in particular $a_i = \alpha_{TP}(T_P - T)$ and $b_i = \alpha_{TA}(T_A - T)$, so they change their sign at virtual Curie temperature T_P and AFE temperature T_A, respectively, $\alpha_{TP,TA} > 0$. All other tensors in Eq. (2) are regarded as temperature-independent. Tensor χ_{ij} is the coupling between the order parameters. The tensors a_{ijk} and b_{ijk}, and the gradient coefficients tensor g_{ijkl} are positively defined for the functional stability. The influence of elastic strain can be approximately taken into account via electrostriction coupling by the renormalization of coefficients in Eq. (2a) (see e.g., [xviii]). Electric field energy is proportional to the background permittivity ε_b of a ferroelectric [viii].

We also need to underline that the expansion coefficients, a_i, b_i, etc., in Eq.(2a) should depend on Zr content x in the compound $Hf_{1-x}Zr_xO_2$, similarly to the x-dependence of $PbZrTiO_3$ expansion coefficients revealed by Haun et al. The x-dependence is most strong for the coefficients $a_i(x,T) = \alpha_{TP}(x)[T_P(x) - T]$ and $b_i(x,T) = \alpha_{TA}(x)[T_A(x) - T]$, because the AFE phase is absent in pure HfO_2 (as well as FE state does not exist in ZrO_2). Knowing this, we can assume that e.g., $a_i(x,T) \sim (1-x)$ and $b_i(x,T) \sim x$. Since we consider the case when x is fixed, we omit the x-dependence in the manuscript.

Below, we use an equation for the surface ionic charge density $\sigma(\phi)$ analogous to the Langmuir adsorption isotherm [xix] and a linear relaxation model to describe the temporal dynamics of the positive (σ_p) and negative (σ_n) surface charge densities:

$$\tau_p \frac{\partial \sigma_p}{\partial t} + \sigma_p = \sigma_{p0}[\phi], \quad \tau_n \frac{\partial \sigma_n}{\partial t} + \sigma_n = \sigma_{n0}[\phi]. \tag{3}$$

where the relation between the relaxation times τ_p and τ_p can be very different due to different mobilities of the ionic and electronic charges. Typically, the relaxation of electrons and/or holes are of the same order, and, at the same time, the relaxation of electrons and holes are much faster that the relaxation of ions. Thus, below we regard that the strong inequalities $\tau_n \ll \tau_p$ or $\tau_p \gg \tau_n$ are valid for the case when the surface charges are electrons and cations, or holes and anions, respectively.

The dependence of equilibrium charge densities $\sigma_{p0}[\phi]$ and $\sigma_{n0}[\phi]$ on the electric potential ϕ is controlled by the concentration of surface ions at the interface $z = 0$, as proposed by Stephenson and Highland [i, ii]:

$$\sigma_{0i}[\phi] = \frac{eZ_i}{N_i}\left(1 + \rho^{-1/n_i} \exp\left(\frac{\Delta G_i^{00} + eZ_i\phi}{k_B T}\right)\right)^{-1}, \tag{4}$$

where e is an elementary charge, Z_i is the ionization degree of the surface ions/electrons, $1/N_i$ are saturation densities of the surface ions. A subscript i designates the summation on positive ($i = p$) and negative ($i = n$) charges, respectively; the dimensionless ratio $\rho = \frac{p_{O2}}{p_{O2}^{00}}$ is the relative partial pressure of oxygen (or other ambient gas), n_i is the number of surface ions created per gas molecule. Two surface charge species exist, since the gas molecule had been electroneutral before its electrochemical decomposition started.

Positive parameters ΔG_1^{00} and ΔG_2^{00} are the free energies of the positive and negative surface charges formation at normal conditions, $p_{O2} = 1$ bar, and zero applied voltage $U = 0$. Specifically, exact values of ΔG_i^{00} are poorly known, as a rule $\Delta G_1^{00} \cong \Delta G_2^{00}$~0.1 eV [49].

Since, as a rule, $\Delta G_n^{00} = \Delta G_p^{00} \cong \Delta G$, $\frac{eZ_n}{N_n} = -\frac{eZ_p}{N_p} = \frac{eZ}{N}$, we obtain from Eq.(4) that $\sigma_{0n}[0] + \sigma_{0p}[0] = \sigma_0[0] = 0$ at normal pressure $\rho = 1$. The condition $\sigma_0[0] = 0$ means that the total screening charge is absent and the surface is electrically-open (or "bare") at normal conditions. Under the UHV $\rho \ll 1$, since $p_{O2} << p_{O2}^{00}$, and so we obtain that $\sigma_0[0] = \frac{eZ}{N}\left(\frac{1}{1+\rho^2 \exp\left(\frac{\Delta G}{k_B T}\right)} - \frac{1}{1+\rho^{-2} \exp\left(\frac{\Delta G}{k_B T}\right)}\right) \cong \frac{eZ}{N}\frac{1}{1+\rho^{-2} \exp\left(\frac{\Delta G}{k_B T}\right)}$, since $n_n = -n_{\mathrm{p}} = 2$ (see Table S1). So, the screening charge exists at zero potential in UHV.

Since the stabilization of a single-domain polarization in ultrathin perovskite films can take place due to the chemical switching [i, ii, xx], we can assume the that the distributions of $P_i(\boldsymbol{r})$ and $A_i(\boldsymbol{r})$ do not deviate significantly from their values averaged over the film thickness. In this case, the behavior of the polarization P_i, anti-polarization A_i, can be described via relaxation-type nonlinear differential equations,

$$\frac{\partial f}{\partial P_i} = -\Gamma_P \frac{\partial P_i}{\partial t}, \quad \frac{\partial f}{\partial A_i} = -\Gamma_A \frac{\partial A_i}{\partial t}. \tag{5}$$

The expression for the out-of-plane electric field E_3 is derived in Ref.[iv]:

$$E_3 = \frac{\Psi}{h} = \frac{\lambda(\sigma_0[\Psi] - P_3) + \varepsilon_0 \varepsilon_d U}{\varepsilon_0(\varepsilon_d h + \lambda \varepsilon_b)}. \tag{6}$$

Eq. (6) corresponds either to the stationary case, or to the adiabatic conditions, when $\sigma_0[\Psi] = \sigma_{0n}[\Psi] + \sigma_{0p}[\Psi]$ in Eq. (3). The overpotential Ψ contains the contribution from surface charges proportional to σ_0, the depolarization field contribution proportional to P_3, and the external potential drop proportional to U. Hence the component E_3 consists of the external field, depolarization field and the field created by the surface ion layer.

The constituent parts of the thermodynamic potential (1) can be further expanded in A_i, P_i and Ψ powers, assuming that $|eZ_i\Psi/k_BT| << 1$. In result we obtain that the surface ionic charge and depolarization field change the coefficients a_3, a_{i3}, χ_{i3}, induce the built-in field E_{SI} and decrease the external "acting" field E_a in the following way:

$$a_3(T, \rho, h) \to a_3\big(1 + S(T, \rho, h)\big) + \frac{\lambda}{2\varepsilon_0(\varepsilon_d h + \lambda \varepsilon_b)}, \tag{7a}$$

$$a_{i3}(T,\rho,h) \to a_{i3}\big(1+S(T,\rho,h)\big), \quad \chi_{i3}(T,\rho,h) \to \chi_{i3}\big(1+S(T,\rho,h)\big), \tag{7b}$$

$$E_3(T,\rho,h) = E_{SI}(T,\rho,h) + E_a(U,h), \tag{7c}$$

$$E_{SI}(T,\rho,h) = \frac{\lambda}{\varepsilon_0(\varepsilon_d h+\lambda\varepsilon_b)}\sum_{i=1,2}\frac{eZ_i}{N_i}f_i(T,\rho), \qquad E_a(U,h) = -\frac{\varepsilon_d U}{\varepsilon_d h+\lambda\varepsilon_b}. \tag{7d}$$

The last term in Eq. (7a), $\frac{\lambda}{2\varepsilon_0(\varepsilon_d h+\lambda\varepsilon_b)}$, originated from the depolarization field. Also, we introduce positive functions in Eq. (7):

$$S(T,\rho,h) = \frac{\lambda\, h}{\varepsilon_0(\varepsilon_d h+\lambda\varepsilon_b)}\sum_{i=1,2}\frac{\left(eZ_i f_i(T,\rho)\right)^2}{N_i k_B T}, \tag{7e}$$

$$f_i(T,\rho) = \left(1+exp\left(\frac{\Delta G_i^{00}}{k_B T}\right)+\rho^{-1/n_i}\right)^{-1}. \tag{7f}$$

It is seen from the expressions (6)-(7) that the solutions of relaxation Eq. (5) depend on the applied voltage U, temperature T, partial oxygen pressure ρ, film thickness h, gap thickness λ, energies ΔG_i^{00} and saturation densities $1/N_i$. Among all LGD coefficients of HZO, the coupling constants χ_{ij} are the most poorly defined parameters.

Note, that analytical expressions (6) - (7) contain the film thickness h in the evident form. Using the expressions, we performed calculations for the range of thickness (5 – 100) nm and reveal an interesting size effect for 5 nm $< h <$10 nm, which may deserve a more detailed theoretical study and experimental verification. However, such small thickness unlikely can be correctly described by a continuous LGD theory, and, without making ab initio calculations, reliable conclusions cannot be made. Because of this, below we limit our consideration by the thickness range $h \geq$10 nm, where the size behavior is the following:

A). The out-of-plane internal electric field E_3 scales as $\frac{\lambda}{h}$, and the acting field E_a is close to an external field, $-\frac{U}{h}$, when $\varepsilon_d h \gg \lambda\varepsilon_b$. This happens for $\lambda \leq$ 0.5 nm, $h \geq$25 nm for typical values $\varepsilon_d = 1$ and $\varepsilon_b = 10$.

B) The scale of thickness-dependent terms in Eq. (7) is also $\frac{\lambda}{h}$. For $\varepsilon_d h \gg \lambda\varepsilon_{33}^b$, the function $S(T,\rho,h) \sim \frac{\lambda\, h}{\varepsilon_0(\varepsilon_d h+\lambda\varepsilon_b)} \sim \frac{\lambda}{\varepsilon_0\varepsilon_d}$ becomes almost thickness-independent. Therefore, the built-in field $E_{SI} \sim \frac{\lambda}{\varepsilon_0(\varepsilon_d h+\lambda\varepsilon_b)} \sim \frac{\lambda}{\varepsilon_0\varepsilon_d h}$ scales as $\frac{\lambda}{h}$. The coefficient a_3, which determines the renormalized Curie temperature, is $a_3 \cong a_0 + \frac{\lambda}{2\varepsilon_0\varepsilon_d h}$; and so its change, $a_3 - a_0$, also scales as $\frac{\lambda}{h}$. So that for $\lambda \leq$ 0.5 nm and $h \geq$10 nm the most important quantities, a_3 and E_{SI}, which behavior determines the film

state, decrease as $\frac{\lambda}{h}$ with h increase. In the case $\frac{\lambda}{h} \ll 0.1$ bulk effects dominate over the contribution of surface ions.

C) Note that the factor $\frac{\lambda}{\varepsilon_0(\varepsilon_d h+\lambda\varepsilon_b)} \sim \frac{\lambda}{h}$, which determines the scaling of a_3 and E_{SI}, originates from the depolarization field. The field suppresses the ferroelectric polar state of the film, and, in order to have a small depolarization field, thick films are required. However, the built-in field E_{SI} and related ionic-induced surface effects also vanish in thick films as $\frac{\lambda}{h}$. Therefore, to reach an optimal balance between bulk and surface effects, we suggest to consider the range of film thickness, $h \cong \frac{\lambda\varepsilon_b}{\varepsilon_d}$.

The analysis of the loops calculated for a simplified 2-4-LGD expansion shows different loop shapes of ferroelectric-like, antiferroelectric-like, and ferroionic types (see **Fig. S2-S7**). The thickness of HZO film is taken $h = 20$ nm, and dimensionless frequency of tip voltage w varies from 10^{-2} to 1. The value $h = 20$ nm is chosen because it is very close to experimental value, 17 nm; however, additional LGD modeling for thickness ranging from 2-20 nm is shown in Fig. S14. Parameters used in calculations are listed in **Table S1.** They were selected in such way to reproduce maximally the experimental results. It is seen from the figures that experimental trends are reproduced qualitatively by the proposed model, but quantitative agreement is not reached.

TABLE S1. Description of physical variables and their numerical values

Description of main physical quantities used in Eqs.(1)-(3)	Designation and dimensionality	Value for a structure $(Hf,Zr)O_2$ film / ionic charge / gap / tip
Coefficient of LGD functional	$a_i = \alpha_{TP}(T_P - T)$ (C^{-2} J m)	T-dependent variable
Dielectric stiffness	α_{TA} ($\times 10^5$ C^{-2}·J·m/K)	2.7969
Curie temperature	T_P (K)	650 (for PZO 463.2)
Coefficient of LGD functional	$b_i = \alpha_{TA}(T_A - T)$ (C^{-2} J m)	T-dependent variable
	α_{TA} ($\times 10^6$ C^{-2}·J·m/K)	4.8789
AFE temperature	T_A (K)	690 (for PZO 490)
Coefficient of LGD functional	a_{11} ($\times 10^8$ J C^{-6}·m^9)	+3.825
Coefficient of LGD functional	b_{11} ($\times 10^9$ J C^{-6}·m^9)	+2.056
Coefficient of LGD functional	χ_{11} ($\times 10^{10}$ J C^{-6}·m^9)	1.7754
Coefficient of LGD functional	a_{111} ($\times 10^9$ J C^{-8}·m^{13})	0
Coefficient of LGD functional	b_{111} ($\times 10^{10}$ J C^{-8}·m^{13})	0
Gradient coefficient	g_{44} ($\times 10^{-10}$ m/F)	(0.5-5)
Kinetic coefficient	Γ (C^{-2} J m s)	rather small
Landau-Khalatnikov relaxation time	τK (s)	10^{-11} – 10^{-13} (far from T_c)

Thickness of ferroelectric layer	h (nm)	(5 – 50), then taken 20 (from experiment)
Background permittivity of ferroelectric	ε_b (dimensionless)	10
Relative oxygen partial pressure	ρ (dimensionless)	(0 - 1) from experiment
Surface charge relaxation times	$\tau_{n,p}$ (s)	>> Landau-Khalatnikov time
Thickness of dielectric gap	λ (nm)	0.4 – 4 (figures are for 0.4 nm)
Permittivity of the dielectric gap	ε_d (dimensionless)	1
Universal dielectric constant	ε_0 (F/m)	8.85×10^{-12}
Electron charge	e (C)	1.6×10^{-19}
Ionization degree of the surface ions	Z_i (dimensionless)	$Z_1 = +2,\ \ Z_2 = -2$
Number of surface ions created per oxygen molecule	n_i (dimensionless)	$n_1 = -2,\ \ n_2 = +2$
Saturation area of the surface ions	N_i (m^2)	10^{-16} - 10^{-18} (for PZO 10^{-18})
Surface defect/ion formation energy	ΔG_i^{00} (eV)	0.01 – 0.2

Note that Landau-Devonshire phenomenology at this level of description does not distinguish between the ferrielectric perovskite PZT and ternary oxide HZO. However, we note the difference in some material parameters, namely in the Curie and AFE temperatures (see Table S1). The material parameters of HZO are mostly unknown, and we used PZO parameters whenever it was possible. The figures S2-S5 have a qualitative sense only, and therefore it appeared impossible to extract more reliable parameters of HZO from the qualitative comparison of the figures with PFM loops.

We would like to draw the readers' attention to **Fig. S2**, plotted for $w = 10^{-2}$ and all the same other parameters as in **Fig. S4**, where $w = 10^{-1}$. One can see how different is the position of the dashed lines separating AFEI, PE and FEI phases on these both figures. The difference is due to the dynamic effects related with different relaxation times of the polarization, electrons and surface ions, e.g., $\tau_n = 10^{-2}\tau_p$. The absolute values of both relaxation times are measured in the units of Landau-Khalatnikov relaxation time, τ_K, which characteristic values are listed in **Table S1.**

So, in contrast to the commonly used thermodynamic phase diagrams, here the phase boundaries significantly depend on the frequency of applied voltage. Basing on the loop opening, we determine the phase boundaries in **Figs. S2** and **S4**. When the loop opening is absent or almost absent, we can regard that it corresponds to the PE phase. Single loops are FEI phase, and double loops are AFEI phase.

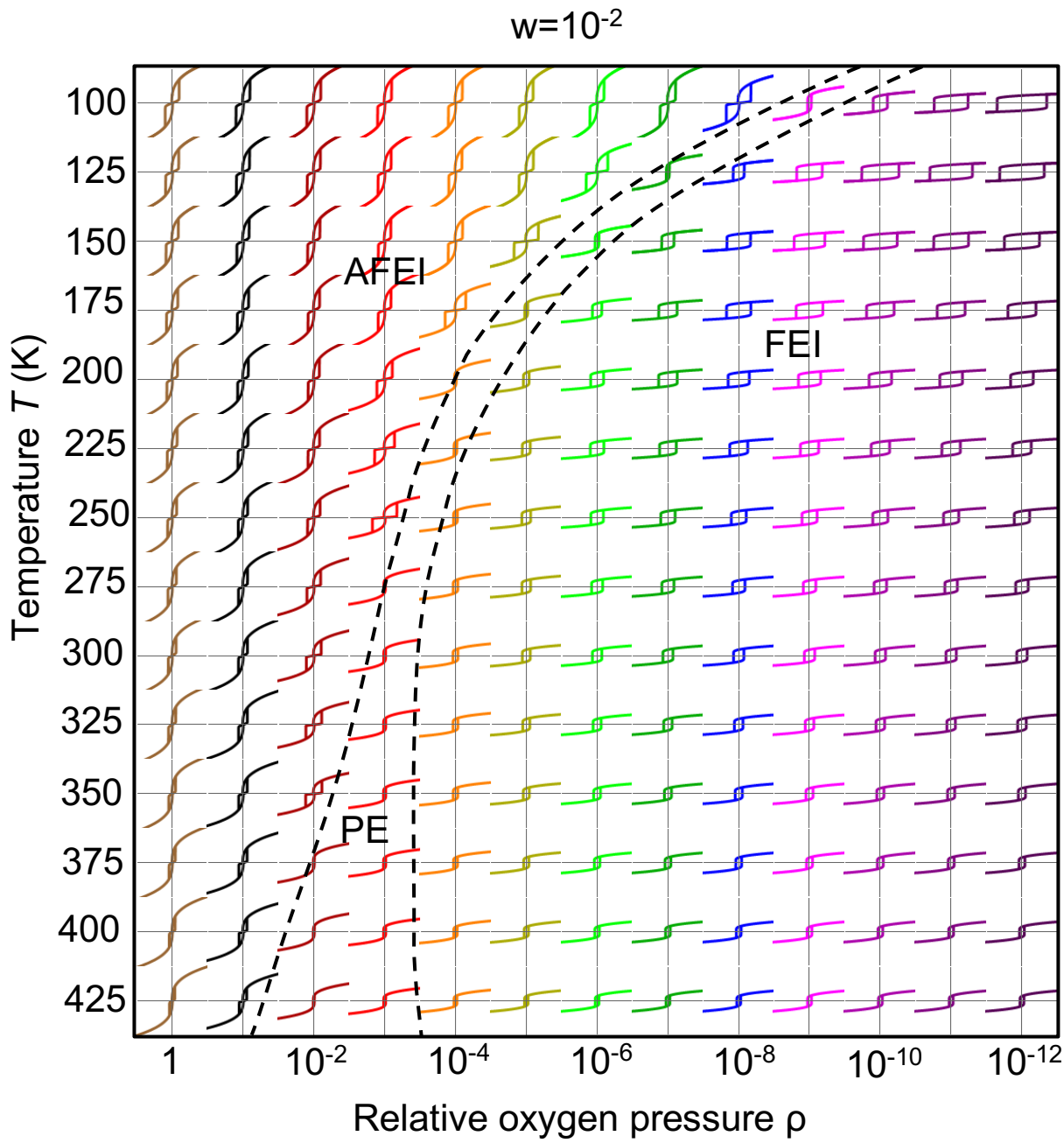

Figure S2. A schematic diagram of the loop shape in dependence on the relative pressure ρ and temperature T. The thickness of HZO film is $h = 20$ nm, and dimensionless frequency of tip voltage $w = 10^{-2}$. Dashed curves separate different type of loops corresponding to the nonpolar AFEI-phase, the intermediate PE-like phase and the FE-like FEI phase. Parameters used in calculations are listed in **Table S1.**

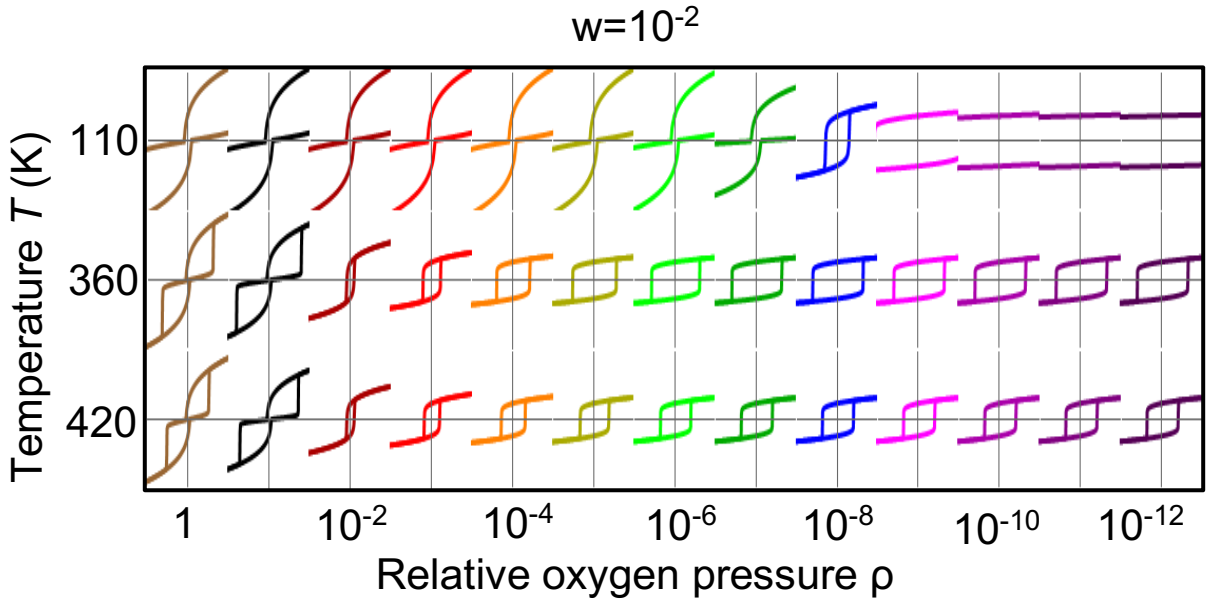

Figure S3. A schematic diagram of the loop shape in dependence on the relative pressure ρ and temperature T. The thickness of HZO film is $h = 20$ nm, and dimensionless frequency of tip voltage $w = 10^{-2}$. Parameters used in calculations are listed in **Table S1.**

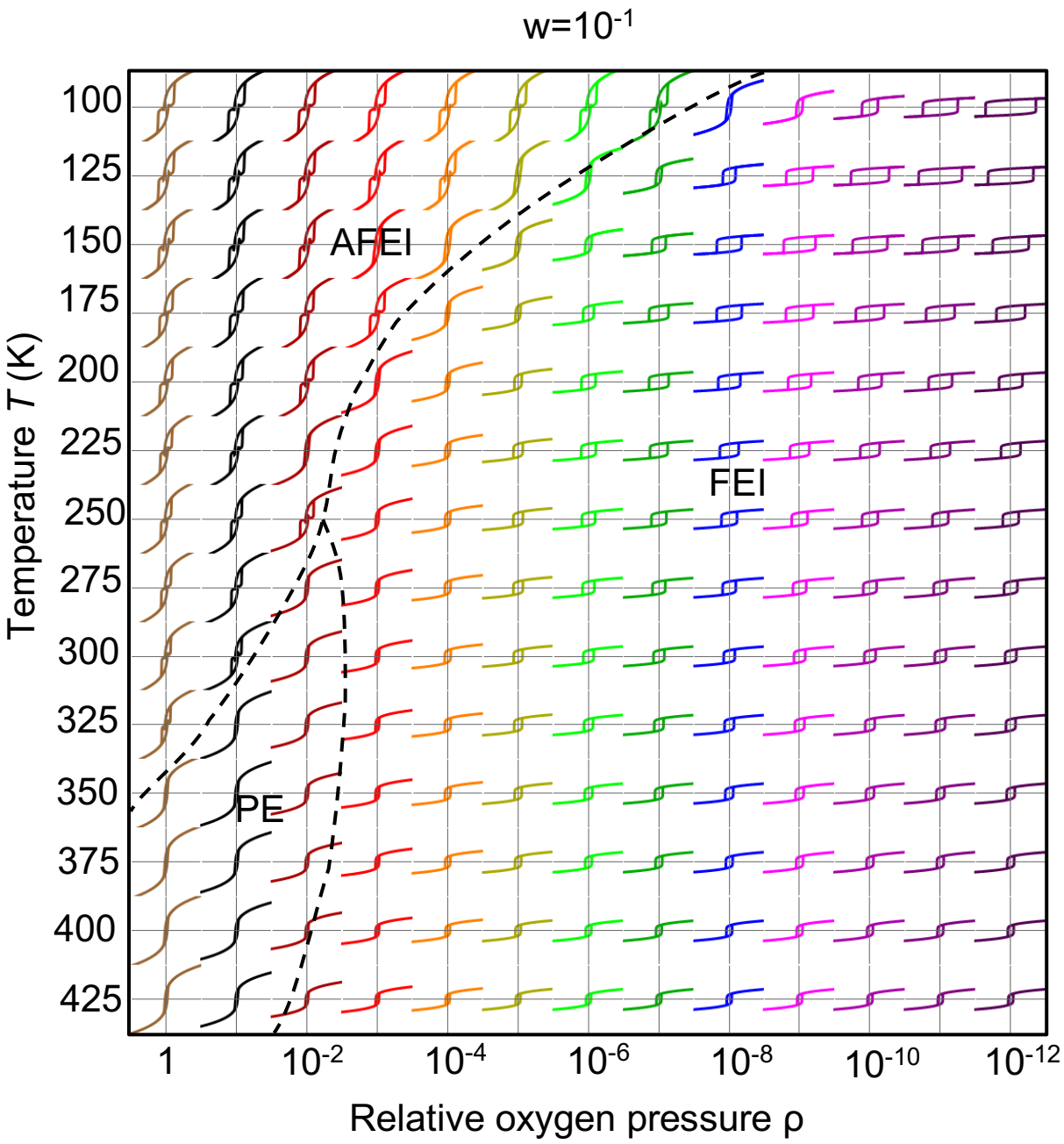

Figure S4. A schematic diagram of the loop shape in dependence on the relative pressure ρ and temperature T. The thickness of HZO film is $h = 20$ nm and dimensionless frequency of tip voltage $w = 10^{-1}$. Dashed curves separate different type of loops corresponding to the nonpolar AFEI-phase, the intermediate PE-like phase and the FE-like FEI phase. Parameters used in calculations are listed in **Table S1.**

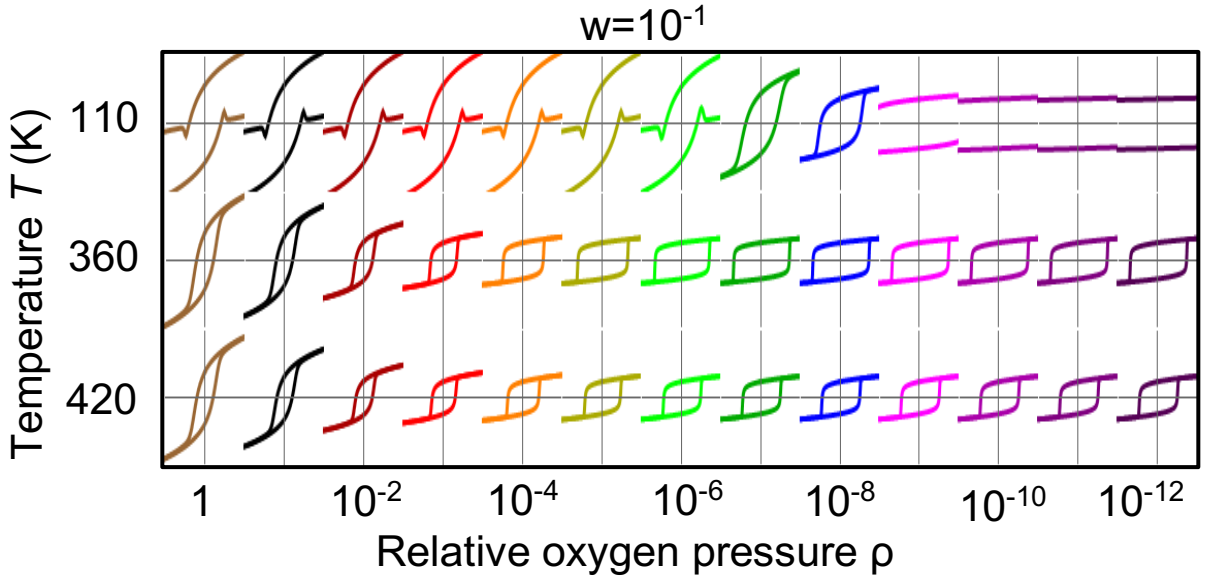

Figure S5. A schematic diagram of the loop shape in dependence on the relative pressure ρ and temperature T. The thickness of HZO film is $h = 20$ nm, dimensionless frequency $w = 10^{-1}$. Parameters used in calculations are listed in **Table S1.**

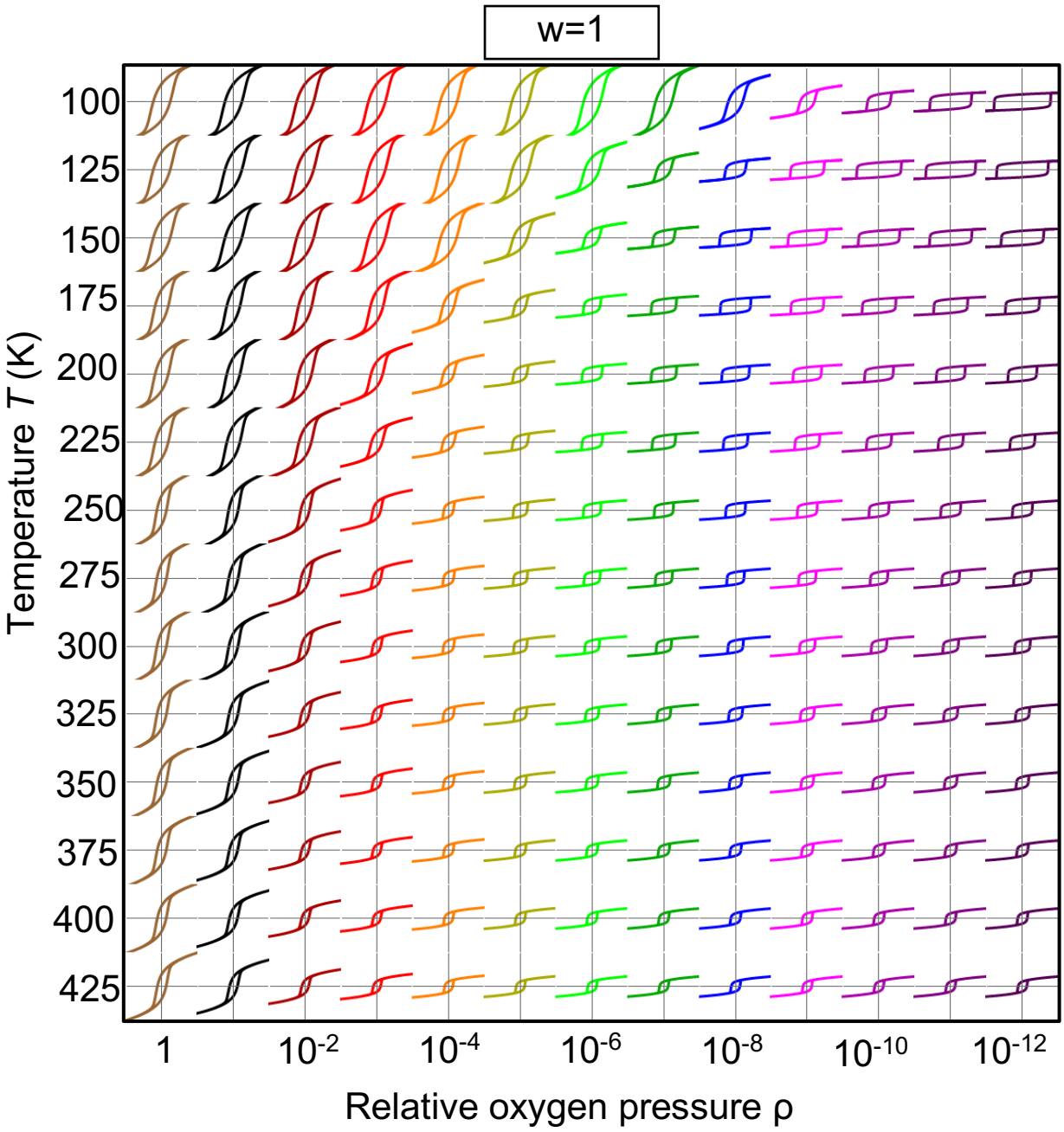

Figure S6. A schematic diagram of the loop shape in dependence on the relative pressure ρ and temperature T. The thickness of HZO film is $h = 20$ nm and dimensionless frequency of tip voltage $w = 1$. Due to the high frequency all loops have a FE-like shape. Parameters used in calculations are listed in **Table S1.**

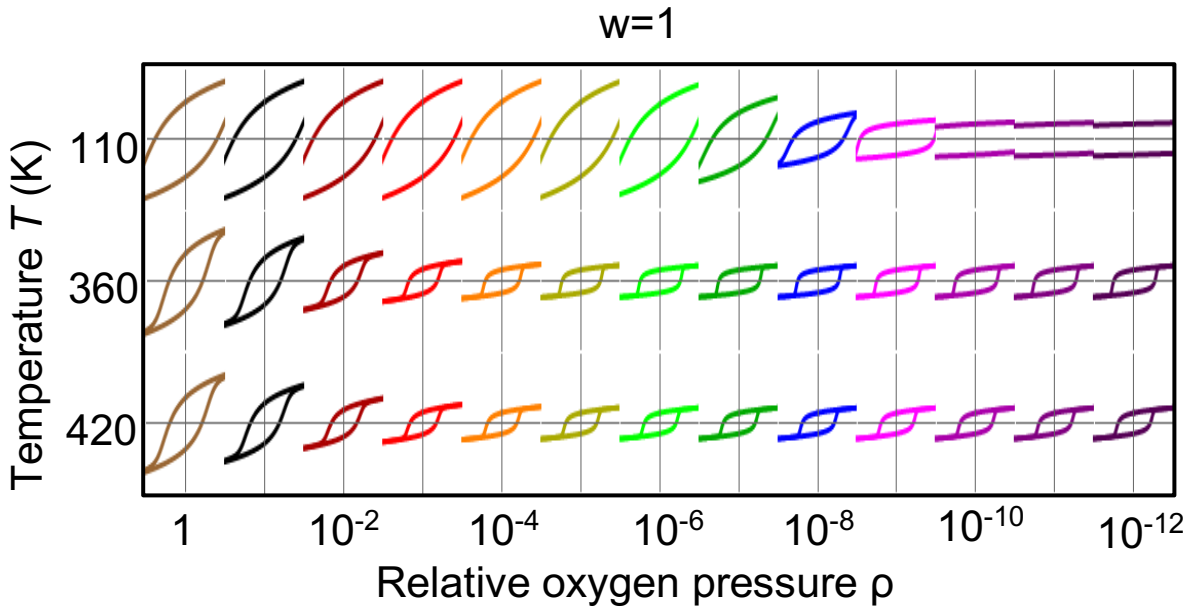

Figure S7. A schematic diagram of the loop shape in dependence on the relative pressure ρ and temperature T. The thickness of HZO film is $h = 20$ nm, dimensionless frequency $w = 1$. Parameters used in calculations are listed in **Table S1.**

C. Additional experimental data

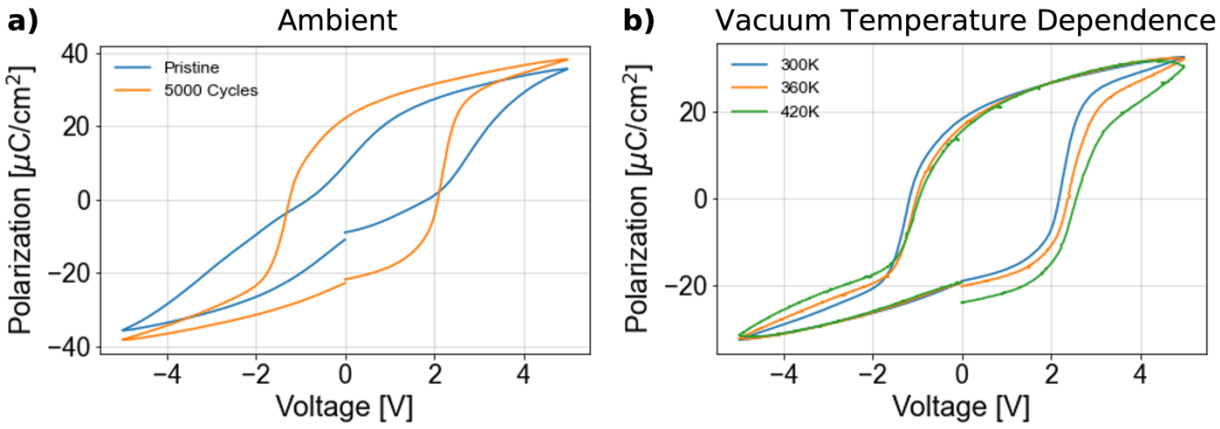

Figure S8. Bulk measurements. Acquired on 17 nm $Hf_{0.5}Zr_{0.5}O_2$ with TaN top electrodes using a Radiant Technologies Precision LC II ferroelectric tester with a measurement period of 1 ms. **(a)** Hysteresis loops were acquired in ambient conditions where blue indicates measurements acquired on pristine $Hf_{0.5}Zr_{0.5}O_2$ and orange indicates measurements acquired on $Hf_{0.5}Zr_{0.5}O_2$ cycled 5000 times with a 2 MV/cm square wave. **(b)** Hysteresis loops were acquired in vacuum post wake-up at 300 K (blue), 360 K (orange), and 420 K (green).

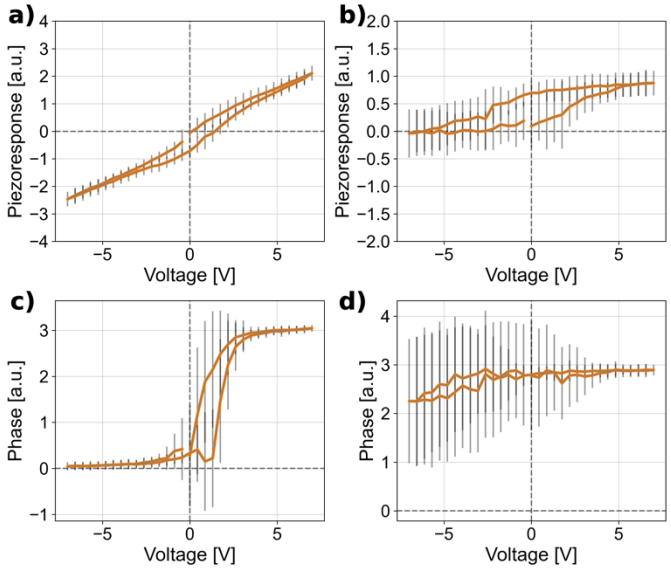

Figure S9. Band excitation PFM acquired in Ar environment. Band excitation PFM acquired from 10x10 grid over 1 μm. (a,b) Piezoresponse and (c,d) phase acquired in the (a,c) on-field and (b,d) off-field state. Note, off-field phase suggests no remanent polarization switching. Data are presented as mean values +/- standard deviation.

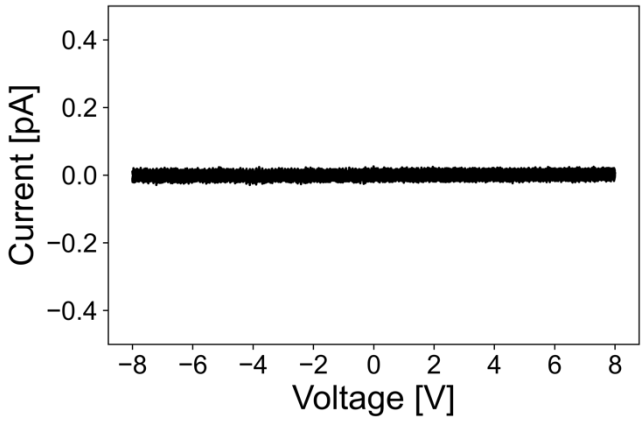

Figure S10. Current-voltage sweep. Current-voltage spectroscopy of 17 nm HZO film acquired on pristine surface in ambient. Note, from -8 V to +8 V negligible current is detected, i.e., the noise floor of the current amplifier.

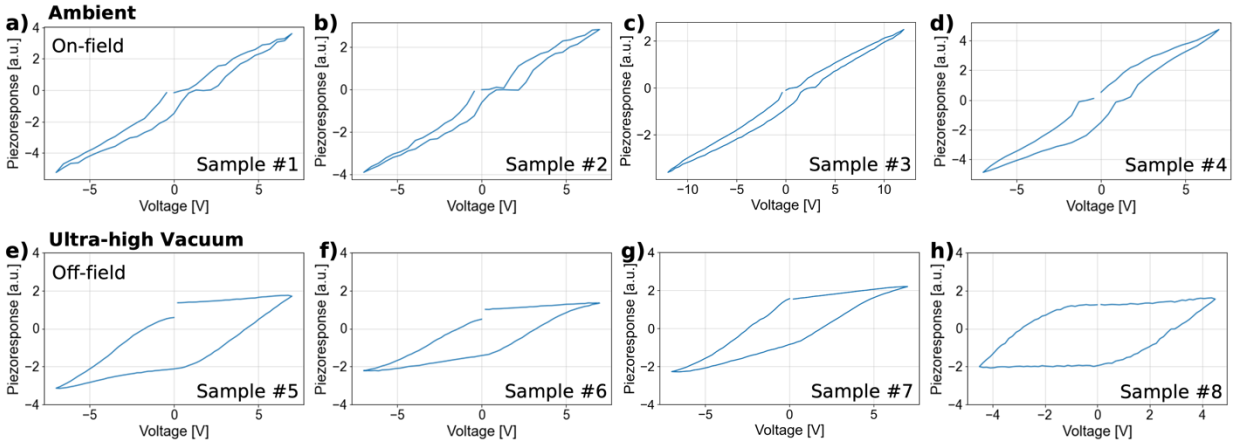

Figure S11. Reproducibility measurements. (a-d) On-field band excitation piezoresponse spectroscopy of four separate $Hf_{0.5}Zr_{0.5}O_2$ thin films (approximately 20 nm thick) acquired in ambient atmosphere. Clear pinching of the hysteresis is observed for all four samples measured in ambient, displaying antiferroelectric behavior. (e-h) Off-field band excitation piezoresponse spectroscopy of four additional $Hf_{0.5}Zr_{0.5}O_2$ thin films (approximately 20 nm thick) acquired in ultra-high vacuum. Square like hysteresis loops are observed without the presence of pinching, displaying ferroelectric behavior. Importantly, all 8 samples were grown independently.

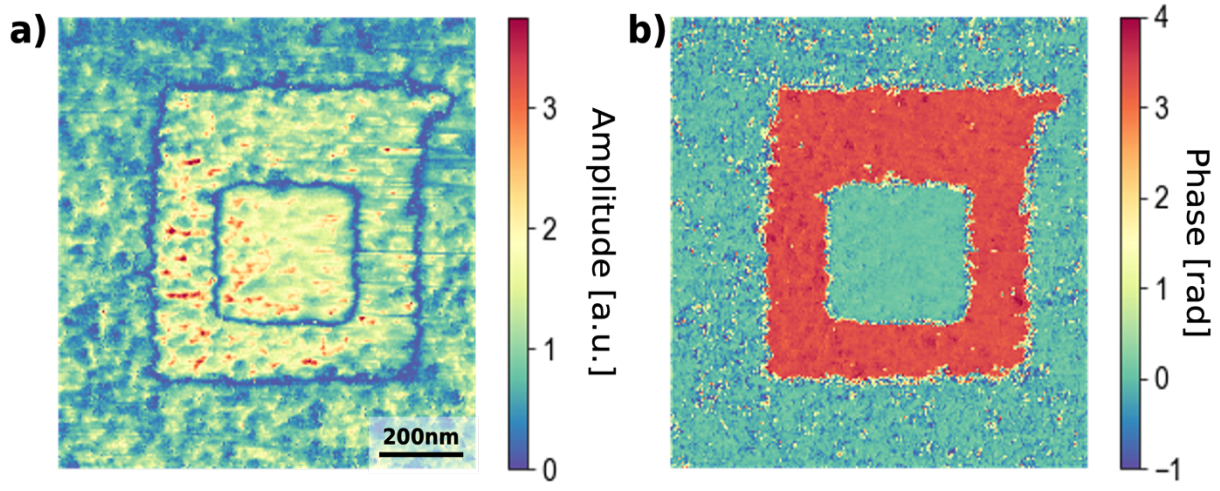

Figure S12. Delayed imaging. Band excitation PFM amplitude (a) and phase (b) acquired approximately 1 hour after poling showing clear ferroelectric domain walls and 180º phase reversal. Note, domains were poled using +7 (larger square) and -7V (smaller square).

D. Thickness scaling in $Hf_{0.5}Zr_{0.5}O_2$

While modeling the interplay between bulk antiferroelectric instability with non-linear surface (or interface) charge compensation is of vital importance for understanding ferroelectricity in HZO, another factor shown to impact the hysteresis loops is thickness scaling. Therefore, we have also modeled the thickness scaling behavior in HZO for thickness greater than 10 nm finding the built-in field (E_{SI}) and change in renormalized Curie temperature, which are dependent on surface ionic charge and depolarization field, scale with λ/h where λ is the ultra-thin gap between the film surface and tip electrode and h is film thickness. Here, the depolarization field suppresses the ferroelectric polar state of the film, and, in order to have a small depolarization field, thick films are required. However, the built-in field and related ionic-induced surface effects also vanish in thick films as λ/h. Thus, to reach an optimal balance between bulk and surface effects, we suggest considering the range of film thickness, $h \cong \frac{\lambda \varepsilon_b}{\varepsilon_d}$ where ε_b and ε_d are the relative background permittivity and the relative permittivity of the ultra-thin gap media, respectively. (Figure S13 and Figure S14).

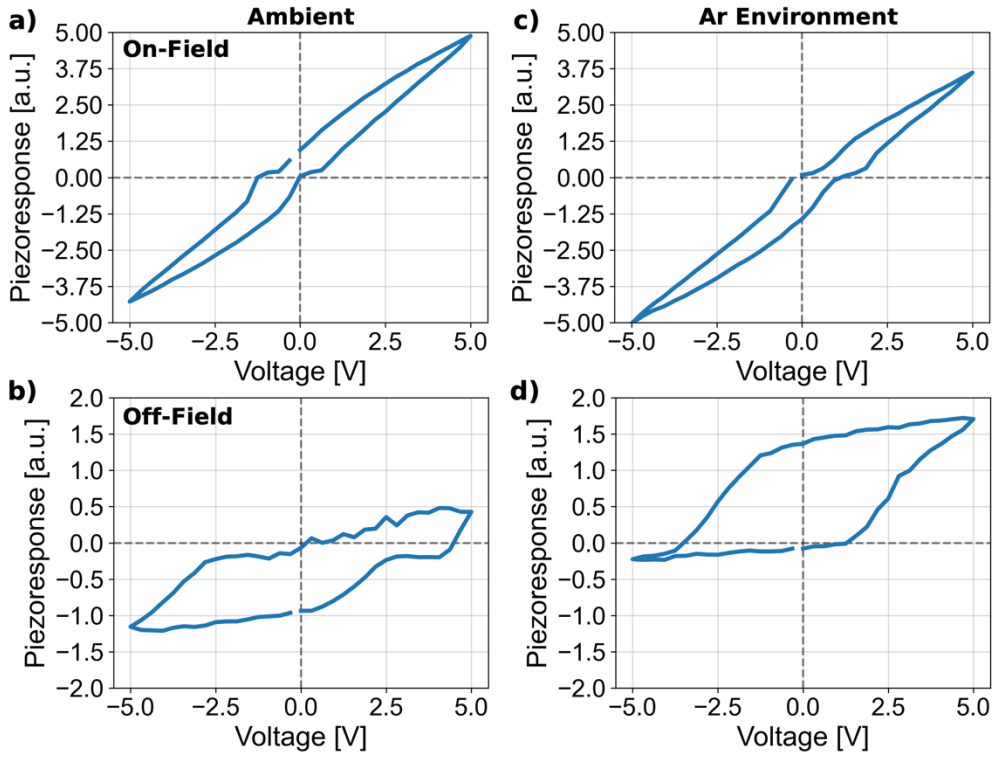

Figure S13: Band excitation piezoresponse spectroscopy hysteresis loops. Average on-field and off-field hysteresis loops of 10 nm $Hf_{0.5}Zr_{0.5}O_2$ over 2 cycles acquired from a 10x10 grid over a 1 μm area in two different environments: (a,b) ambient and (c,d) argon. Top (a,c) and bottom (b,d) panels correspond to on-field and off-field hysteresis loop, respectively.

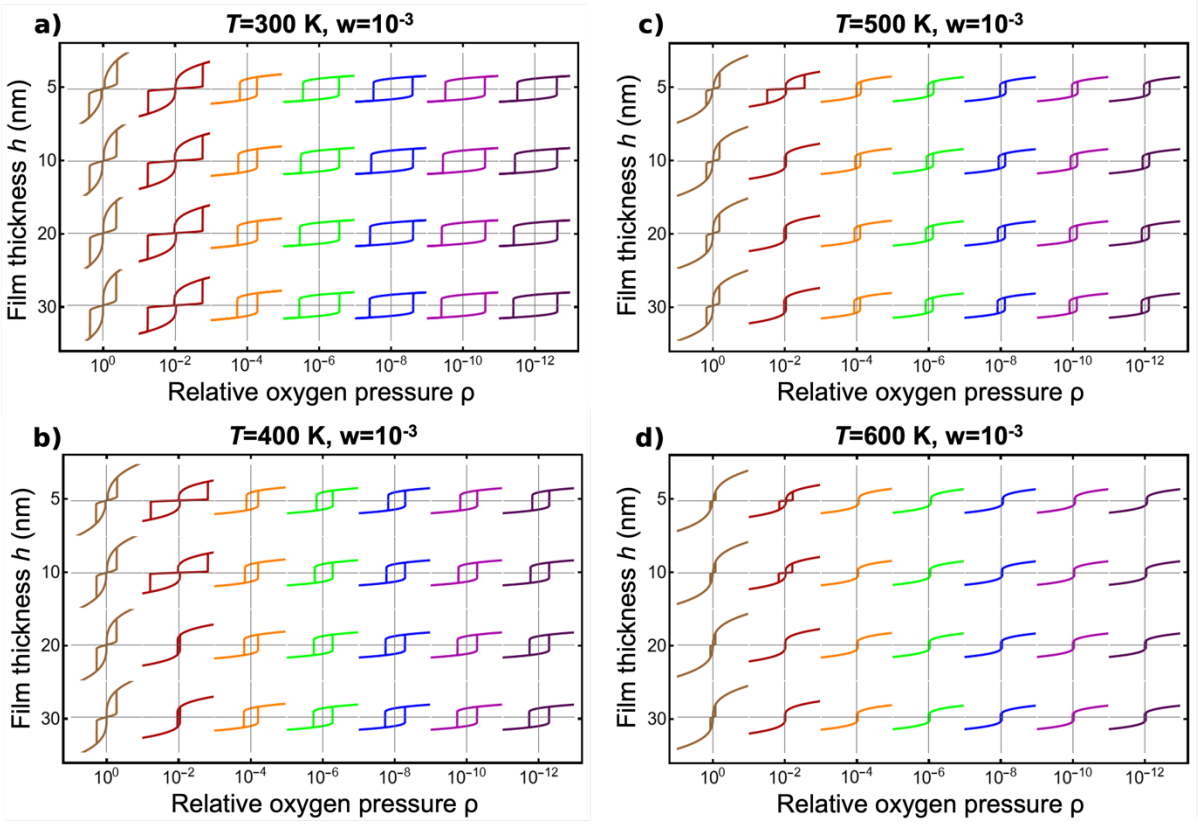

Figure S14: A schematic diagram of the loop shape dependence on the relative oxygen pressure ρ and (Hf,Zr)O_2 thickness h. Panels (a-d) are modeled for temperatures 300 K, 400 K, 500 K, and 600 K respectively. The dimensionless frequency of tip voltage $w = 10^{-3}$. Parameters used in calculations are listed in Table S1.

E. Scanning transmission electron microscopy discussion

A tetragonal phase oriented along the [100] zone axis could contribute to the symmetry in the PACBED. However, the coexistence of the polar *Pca*2_1 and the antipolar *Pbca* phases is uniquely determined through the combination of atomic resolution images, their FFT patterns, and the PACBED patterns. Figure S13 shows the simulated diffraction patterns, the PACBED and the STEM image simulations for the three phases, each of which could partially fit the experimental results. No other orientation of these phases has been identified as a good match for the experimental results. Although the experimental atomic-resolution HAADF images match any of

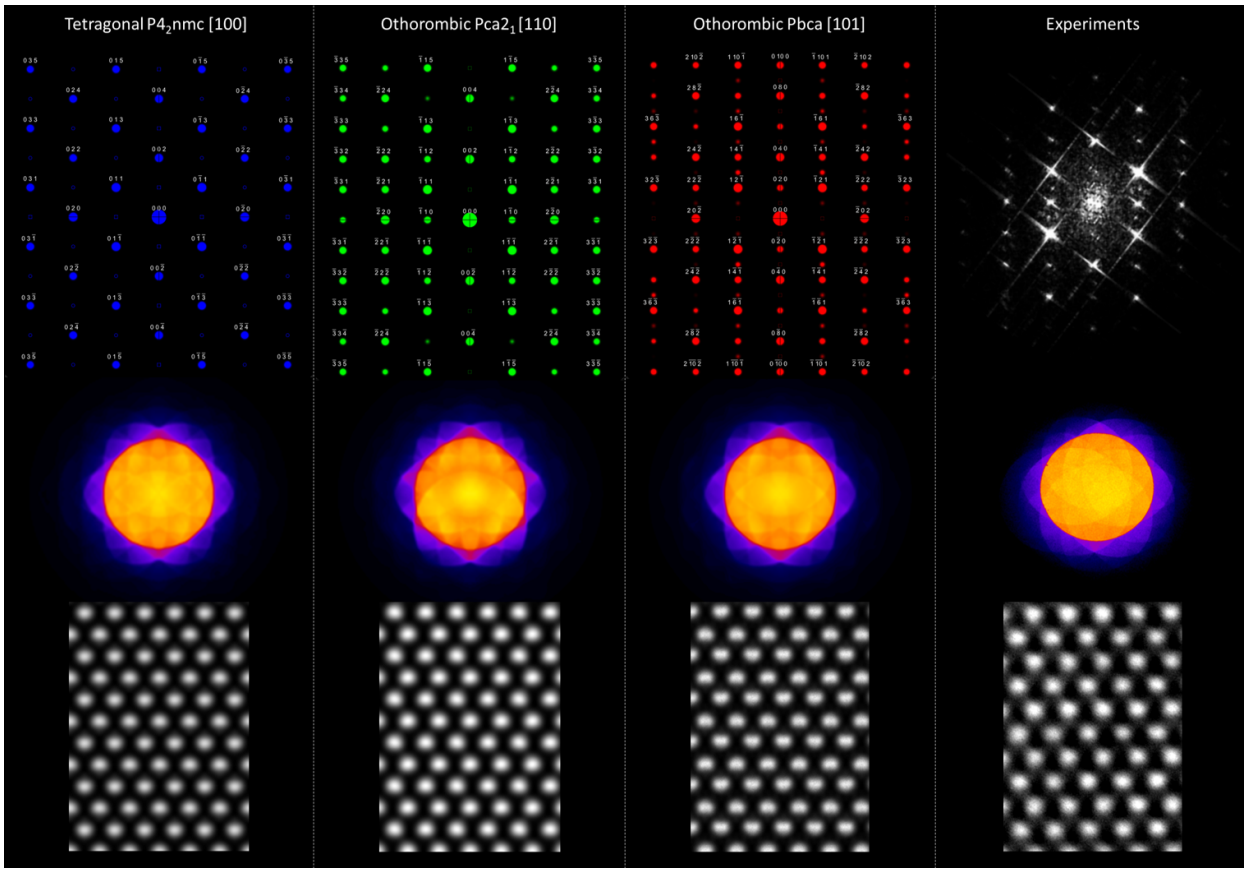

Figure S15. Comparison of modeled and experimental STEM results. Modeled tetragonal P4_2nmc [100], modeled orthorhombic *Pca*2_1 [110], modeled orthorhombic *Pbca* [101], and experimental results. For each modeled phase, the FFT patterns, simulated position-averaged convergent beam electron diffraction (PACBED) patterns, and simulated STEM images are shown from top to bottom, respectively. Correspondingly, experimental FFT, PACBED patterns, and HAADF images are shown on the far right.

these three phases, the main reflections in the FFT can be attributed to any of the three phases, while the dimmer reflections can only be attributed to the antipolar *Pbca* phase. This information, in addition to the lack of mirror plane in the PABED, which can only be attributed to polar $Pca2_1$ phase, provide the evidence that the two orthorhombic phases coexist within the grains; this is the only interpretation consistent with our experimental data, and the interpretation agrees with the observations of Y. Cheng et al. *Nat. Commun.* 2022, 13 (1), 645 (reference 53, main text).

It is important to note, the orientation of the modeled phases were chosen based on the symmetry observed in the experimental atomic resolution images and corresponding FFTs, from which the interatomic distances were calculated and matched with the modelled phases and following the rules for indexing electron diffraction patterns. This follows the standard crystallographic reference axes for these phases as summarized below:

Table S2. Non-polar phase Pbca crystallographic reference axes

Space Group:	*P b c a*
Crystal System:	Orthorhombic
a:	5.0857 Å
b:	10.0588 Å
c:	5.2484 Å

Table S3. Polar phase $Pca2_1$ crystallographic reference axes

Space Group:	*P c a* 2_1
Crystal System:	Orthorhombic
a:	5.2693 Å
b:	5.0401 Å
c:	5.0745 Å

F. Local switching dynamics via band excitation PFM in UHV

To gain further insight into the localized ferroelectric switching dynamics in HZO observed under low environmental oxygen partial pressure, we perform a high density 50x50 spectroscopy grid (Figure S16) over a 500 nm region in UHV, approaching the resolution limit of PFM. Figure S16a,b shows the amplitude and phase at t=0 (0 V) where clear inhomogeneous response can be observed. Here, we aim to evaluate the hysteresis loops in selective regions to deconvolve the spatially inhomogeneous response. As such, we apply a threshold mask (amplitudes greater than 0.2) to Figure S16a to isolate the higher response regions, shown as the masked purple regions in

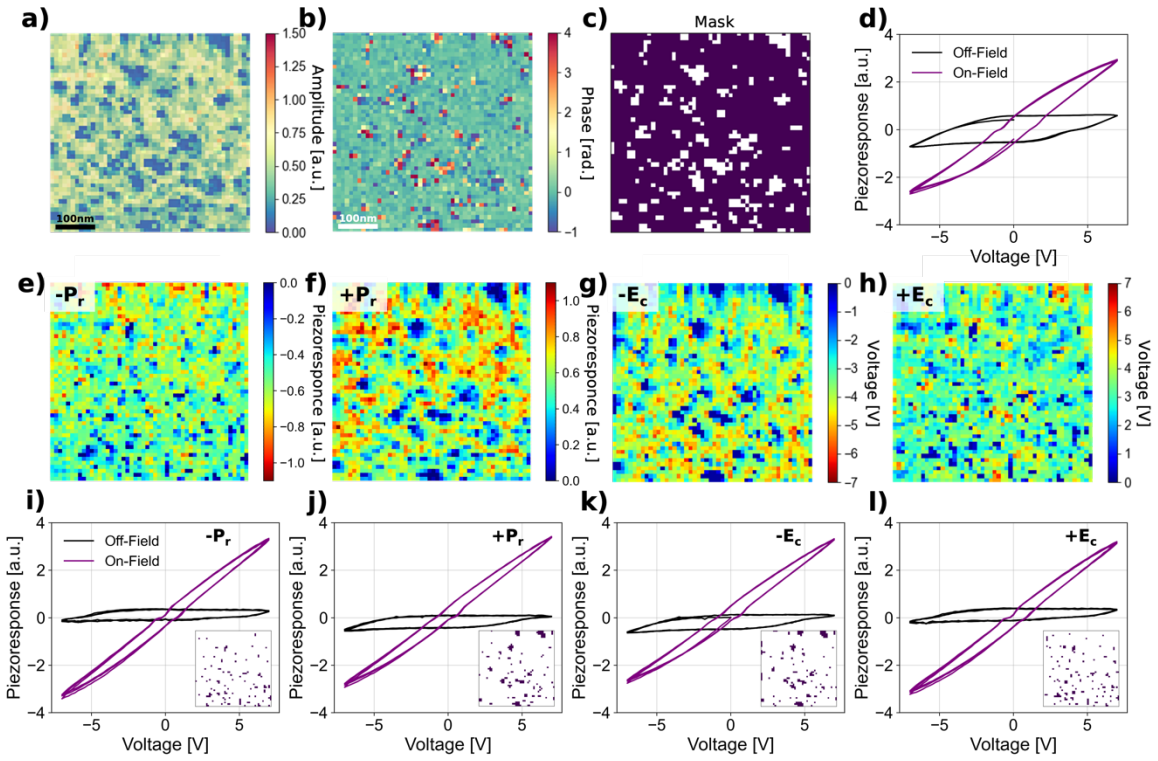

Figure S16. High density band excitation piezoresponse spectroscopy in ultra-high vacuum. BE piezoresponse spectroscopy off-field **(a)** amplitude and **(b)** phase of 50x50 high density spectroscopy grid acquired over 500 nm at $V,t = 0$ (V,s). **(c)** Masked off-field amplitude using a threshold of 0.2 to identify regions of higher response and **(d)** corresponding average on-field and off-field (purple, black respectively) hysteresis loops. **(e,f)** Remanent piezoresponse and **(g,h)** coercive field maps derived from high density spectroscopy grid in the off-field state. **(i-l)** Average loops acquired from masked regions determined from thresholding remanent piezoresponse and coercive field maps, i.e. low P_r and E_c regions.

Figure S16c. The average on-field and off-field response from the masked region is shown in Figure S16d. Importantly, the masked regions show a similar response to Figure 3c,f (i.e. ferroelectric switching).

Next, we calculate remanent piezoresponse, P_r, and coercive field, E_c, maps from the dense spectroscopy grid (in the off-field state) determined by the zero bias and zero piezoresponse crossings, respectively, yielding four maps: $-P_r$, $+P_r$, $-E_c$, and $+E_c$ (Figure 4e-h). Qualitatively, the regions of low remanent piezoresponse and coercive field are in good agreement with the initial low response regions observed in Figure S16a. To identify the localized switching behavior of these regions, i.e. blue clusters in Figure S16e-h, we threshold the remanent piezoresponse and

coercive field maps to isolate the regions (similar to the methodology employed in Figure S16c) and plot the corresponding average hysteresis loops (see Methods Section). Interestingly, regions of low $-P_r$ and $+E_c$, and low $+P_r$ and $-E_c$ are spatially correlated as seen in Figure S16e,h and Figure S16f,g respectively. Furthermore, the average on-field and off-field hysteresis loops derived from these regions are strikingly similar. Specifically, for regions of low $-P_r/+E_c$, the average on-field loop has a high degree of pinching isolated to the negative branch of the loop, while the average off-field loop shows mostly positive piezoresponse. In contrast, in the regions of low $+P_r/-E_c$, the average on-field loop has a high degree of pinching isolated to the positive branch of the loop, while the average off-field loop exhibits mostly negative piezoresponse. Here, we posit at 300 K in UHV, the HZO thin film is on the boundary of antiferroelectric instability where the observed spatial inhomogeneities suggest the presence of localized antiferroic states, or crystallographic phases.

i Stephenson, G. B.; Highland, M. J. Equilibrium and Stability of Polarization in Ultrathin Ferroelectric Films with Ionic Surface Compensation. *Phys. Rev. B* **2011**, *84* (6), 064107. https://doi.org/10.1103/PhysRevB.84.064107.

ii Highland, M. J.; Fister, T. T.; Fong, D. D.; Fuoss, P. H.; Thompson, C.; Eastman, J. A.; Streiffer, S. K.; Stephenson, G. B. Equilibrium Polarization of Ultrathin PbTiO3 with Surface Compensation Controlled by Oxygen Partial Pressure. *Phys. Rev. Lett.* **2011**, *107* (18), 187602. https://doi.org/10.1103/PhysRevLett.107.187602.

iii Yang, S. M.; Morozovska, A. N.; Kumar, R.; Eliseev, E. A.; Cao, Y.; Mazet, L.; Balke, N.; Jesse, S.; Vasudevan, R. K.; Dubourdieu, C.; Kalinin, S. V. Mixed Electrochemical–Ferroelectric States in Nanoscale Ferroelectrics. *Nature Phys* **2017**, *13* (8), 812–818. https://doi.org/10.1038/nphys4103.

iv Morozovska, A. N.; Eliseev, E. A.; Morozovsky, N. V.; Kalinin, S. V. Ferroionic States in Ferroelectric Thin Films. *Phys. Rev. B* **2017**, *95* (19), 195413. https://doi.org/10.1103/PhysRevB.95.195413.

v Morozovska, A. N.; Eliseev, E. A.; Morozovsky, N. V.; Kalinin, S. V. Piezoresponse of Ferroelectric Films in Ferroionic States: Time and Voltage Dynamics. *Appl. Phys. Lett.* **2017**, *110* (18), 182907. https://doi.org/10.1063/1.4979824.

vi Morozovska, A. N.; Eliseev, E. A.; Kurchak, A. I.; Morozovsky, N. V.; Vasudevan, R. K.; Strikha, M. V.; Kalinin, S. V. Effect of Surface Ionic Screening on the Polarization Reversal Scenario in Ferroelectric Thin Films: Crossover from Ferroionic to Antiferroionic States. *Phys. Rev. B* **2017**, *96* (24), 245405. https://doi.org/10.1103/PhysRevB.96.245405.

vii A. N. Morozovska, E. A. Eliseev, A. Biswas, N. V. Morozovsky, and S. V. Kalinin. Effect of surface ionic screening on polarization reversal and phase diagrams in thin antiferroelectric films for information and energy storage. Phys. Rev. Applied 16, 044053 (2021)

[viii] A.K. Tagantsev, L.E. Cross, and J. Fousek, *Domains in ferroic crystals and thin films* (Springer, New York, 2010).

[ix] A.M. Bratkovsky, and A.P. Levanyuk. Continuous theory of ferroelectric states in ultrathin films with real electrodes. J. Comput. Theor. Nanoscience **6**, 465 (2009).

[x] A.K. Tagantsev and G. Gerra. Interface-induced phenomena in polarization response of ferroelectric thin films. J. Appl. Phys. **100**, 051607 (2006).

xi Tagantsev, A. K.; Gerra, G. Interface-Induced Phenomena in Polarization Response of Ferroelectric Thin Films. *Journal of Applied Physics* **2006**, *100* (5), 051607. https://doi.org/10.1063/1.2337009.

[xii] M.J. Haun, T.J. Harvin, M.T. Lanagan, Z.Q. Zhuang, S.J. Jang, and L.E. Cross. Thermodynamic theory of $PbZrO_3$, J. Appl. Phys. **65**, 3173 (1989).

[xiii] M.J. Haun, Z.Q. Zhuang, E. Furman, S.J. Jang, and L.E. Cross, Thermodynamic theory of the lead zirconate-titanate solid solution system, Part III: Curie constant and sixth-order polarization interaction dielectric stiffness coefficients, Ferroelectrics, **99**, 45 (1989).

xiv Blinc, R.; Zeks, B. *Soft Mode in Ferroelectrics and Antiferroelectrics*; North-Holland Publishing Company, Amsterdam, Oxford, 1974.

xv Tagantsev, A. K.; Vaideeswaran, K.; Vakhrushev, S. B.; Filimonov, A. V.; Burkovsky, R. G.; Shaganov, A.; Andronikova, D.; Rudskoy, A. I.; Baron, A. Q. R.; Uchiyama, H.; Chernyshov, D.; Bosak, A.; Ujma, Z.; Roleder, K.; Majchrowski, A.; Ko, J.-H.; Setter, N. The Origin of Antiferroelectricity in PbZrO3. *Nat Commun* **2013**, *4* (1), 2229. https://doi.org/10.1038/ncomms3229.

xvi Rabe, K. M. Antiferroelectricity in Oxides: A Reexamination. In *Functional Metal Oxides*; John Wiley & Sons, Ltd; pp 221–244. https://doi.org/10.1002/9783527654864.ch7.

xvii Hlinka, J.; Ostapchuk, T.; Buixaderas, E.; Kadlec, C.; Kuzel, P.; Gregora, I.; Kroupa, J.; Savinov, M.; Klic, A.; Drahokoupil, J.; Etxebarria, I.; Dec, J. Multiple Soft-Mode Vibrations of Lead Zirconate. *Phys. Rev. Lett.* **2014**, *112* (19), 197601. https://doi.org/10.1103/PhysRevLett.112.197601.

xviii Tagantsev, A.; Cross, L. E.; Fousek, J. *Domains in Ferroic Crystals and Thin Films*; Springer: New York, 2010.

xix Foo, K. Y.; Hameed, B. H. Insights into the Modeling of Adsorption Isotherm Systems. *Chemical Engineering Journal* **2010**, *156* (1), 2–10. https://doi.org/10.1016/j.cej.2009.09.013.

xx Cao, Y.; Kalinin, S. V. Phase-Field Modeling of Chemical Control of Polarization Stability and Switching Dynamics in Ferroelectric Thin Films. *Phys. Rev. B* **2016**, *94* (23), 235444. https://doi.org/10.1103/PhysRevB.94.235444.